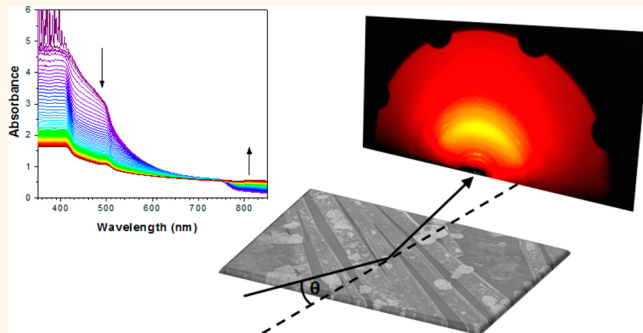


Investigation of $\text{CH}_3\text{NH}_3\text{PbI}_3$ Degradation Rates and Mechanisms in Controlled Humidity Environments Using *in Situ* Techniques

Jinli Yang, Braden D. Siempelkamp, Dianyi Liu, and Timothy L. Kelly*

Department of Chemistry, University of Saskatchewan, 110 Science Place, Saskatoon, SK Canada, S7N 5C9

ABSTRACT Perovskite solar cells have rapidly advanced to the forefront of solution-processable photovoltaic devices, but the $\text{CH}_3\text{NH}_3\text{PbI}_3$ semiconductor decomposes rapidly in moist air, limiting their commercial utility. In this work, we report a quantitative and systematic investigation of perovskite degradation processes. By carefully controlling the relative humidity of an environmental chamber and using *in situ* absorption spectroscopy and *in situ* grazing incidence X-ray diffraction to monitor phase changes in perovskite degradation process, we demonstrate the formation of a hydrated intermediate containing isolated PbI_6^{4-} octahedra as the first step of the degradation mechanism. We also show that the identity of the hole transport layer can have a dramatic impact on the stability of the underlying perovskite film, suggesting a route toward perovskite solar cells with long device lifetimes and a resistance to humidity.



KEYWORDS: perovskites · relative humidity · moisture · decomposition · GIXRD

Since the seminal work of Miyasaka *et al.*,¹ photovoltaic devices based on organometal halide perovskites of the family $\text{CH}_3\text{NH}_3\text{PbX}_3$ ($X = \text{I}^-, \text{Br}^-, \text{Cl}^-$) have experienced incredibly rapid improvements in performance, with power conversion efficiencies (PCEs) rising from 3.8% to 19.3% in just five years.^{2–11} These perovskite-structured semiconductors have benefitted from physical properties ideally suited to photovoltaics, including direct band gaps, long charge carrier diffusion lengths and low carrier effective masses, high absorption coefficients, defect tolerance, and compatibility with low-cost, solution-based fabrication processes.^{12–15} This has allowed these compounds to be integrated into a variety of device architectures, including both mesoscopic devices^{3,5,8–10,16} and planar heterojunctions.^{17–19}

Despite accommodating a wide variety of cell designs and producing excellent PCEs, perovskite solar cells must first overcome a number of technical issues before widespread commercialization is possible. These

include scale-up of the cell area, the toxicity of lead, and a lack of long-term device stability.²⁰ Efforts to address these shortcomings have begun to show promise, with *ca.* 1 cm^2 perovskite devices producing efficiencies as high as 8.3%²¹ and lead-free perovskite solar cells having now been reported.^{22,23} Despite this progress, the instability of the $\text{CH}_3\text{NH}_3\text{PbI}_3$ semiconductor remains a major obstacle to commercialization.^{10,24–26} In the presence of moisture, the dark brown $\text{CH}_3\text{NH}_3\text{PbI}_3$ perovskite undergoes rapid decomposition to PbI_2 , resulting in a significant decline in device performance.^{24,26} For unencapsulated perovskite solar cells, Zhou *et al.*¹⁰ reported an 80% drop in PCE over a 24 h period when the cells were left stored under ambient conditions and a 95% drop in PCE after 6 days. While this loss in performance is highly problematic, even more concerning is that the decomposition product (PbI_2) is sparingly soluble in water (1.6 mM at 25 °C),²⁷ this would present an enormous ecotoxicological problem if a module were to become damaged in the field.

* Address correspondence to tim.kelly@usask.ca.

Received for review December 2, 2014 and accepted January 30, 2015.

Published online January 30, 2015
10.1021/nn506864k

© 2015 American Chemical Society

Given these issues, substantial effort has gone into improving the long-term stability of perovskite solar cells.^{25,28–35} Protective Al₂O₃ layers²⁸ and hydrophobic oligothiophene hole transport layers (HTLs)²⁹ have both been employed as a means of protecting the underlying perovskite film, while alternative perovskite compositions^{30,31} have also been explored as a way of improving the stability of the perovskite itself. However, some of the most promising results have come from the use of carbon-based electrodes.^{25,32–35} Wei *et al.*³⁴ used inkjet printing to produce CH₃NH₃PbI₃/C bilayer devices, which retained *ca.* 90% of their initial PCE after storage in 30% relative humidity (RH) for 12 days. Similarly, Zhang *et al.*³³ and Zhou *et al.*³⁵ replaced the typical Ag or Au back-contact with carbon paste deposited by doctor-blading. The unencapsulated devices were stable for up to 2000 h in air, with the thick carbon paste protecting the perovskite from ambient humidity. Most dramatically, through the use of functionalized carbon nanotubes embedded in an insulating polymer matrix, Habisreutinger *et al.*²⁵ were able to protect perovskite devices from a steady stream of running water for a short time.

Although some improvements have been made in the stability of perovskite solar cells, there is actually very little known about either the degradation rate or decomposition mechanism of the CH₃NH₃PbI₃ perovskite upon exposure to moisture. Studies on perovskite stability have typically been carried out under “ambient” conditions; however, without tight environmental controls, the relative humidity will vary widely as the result of both short-term and seasonal weather variations. This makes it exceptionally difficult to draw meaningful comparisons between experiments carried out in different laboratories, limiting the ability to gain meaningful mechanistic insight into decomposition processes. In this work, we report a quantitative and systematic investigation of perovskite degradation processes. By carefully controlling the RH of an environmental chamber and using *in situ* absorption spectroscopy and *in situ* grazing incidence X-ray diffraction (GIXRD) to monitor changes in the perovskite crystallinity and electronic structure, we are able to gain important insights into the inherent moisture stability of CH₃NH₃PbI₃, as well as the role of various device components in protecting the perovskite from hydrolysis.

RESULTS AND DISCUSSION

In order to reproducibly measure the decomposition rate of perovskite films as a function of RH, we built an experimental setup to produce a constant flow of gas with the desired RH, as shown in Figure 1. The RH is controlled by adjusting the relative flow rates of saturated water vapor and diluent carrier gas (Figure 1a), and a RH sensor placed downstream of the custom-built sample holder (Figure 1b) allows continual

monitoring of the actual humidity in the sample cell. This arrangement enabled the acquisition of *in situ* UV-vis absorbance measurements during the decomposition process. Absorbance measurements made on perovskite films *ex situ* (Figure S1) show the expected spectral features of CH₃NH₃PbI₃: namely, an intense high-energy absorption band below 500 nm and an optical band gap of *ca.* 760 nm. After long-term exposure to ambient air, the absorption onset at 760 nm is no longer visible, and the remaining spectral features closely resemble those of PbI₂. This transformation is more apparent in the *in situ* absorbance data obtained at 98 ± 2% relative humidity (Figure 1c). The high-energy absorption features below 500 nm show an immediate and rapid bleach upon exposure to moisture, while the band gap at 760 nm is also steadily eroded. There is also a concomitant increase in the background absorbance ($\lambda > 800$ nm) due to increased levels of Mie scattering³⁶ within the film, indicating the formation of large crystallites as part of the decomposition process. In order to better quantify the rate of decomposition, the absorbance at 410 nm (where the largest changes in optical density are observed) was plotted against time, and the results were compared with normalized data acquired at 80%, 50%, and 20% RH (Figure 1d). The expected trend of faster decomposition at higher humidities was observed; defining $\tau_{1/2}$ as the point at which the normalized absorbance was halfway between its initial (1.00) and final (~0.33) values, $\tau_{1/2} \approx 4$ h for the highest RH (98%), whereas $\tau_{1/2} \approx 34$ h at 80% RH. At lower RH, the decomposition process was quite slow; extrapolation of a linear fit of the 50% and 20% RH data from Figure 1d suggests that $\tau_{1/2} \approx 1000$ and 10 000 h, respectively (Figure S2). This is highly encouraging from the perspective of device stability; since the perovskite absorber appears able to tolerate small quantities of moisture (<20% RH), it suggests that lower quality (and therefore less expensive) encapsulation strategies may be enough to stabilize perovskite solar cells and prevent device degradation.

The effect of carrier gas on the stability of the perovskite film was also investigated. Perovskite films were exposed to a 98% RH gas flow, using both air and nitrogen as the carrier gas (Figure S3). There was no appreciable change in the degradation rate, with $\tau_{1/2} \approx 2$ –4 h in both cases. The results were also quite reproducible, with relatively little variation in $\tau_{1/2}$ from sample to sample. Additionally, perovskite films sealed in the holder under a constant flow of dry air (0% RH) showed no change in the absorption spectrum (Figure S4) over the course of 2 weeks, indicating that oxygen has little to no effect on the degradation of the perovskite and that it is the moisture in the ambient environment that is the primary cause of perovskite degradation.

Given that moisture was identified as the main culprit in perovskite decomposition, we wanted to

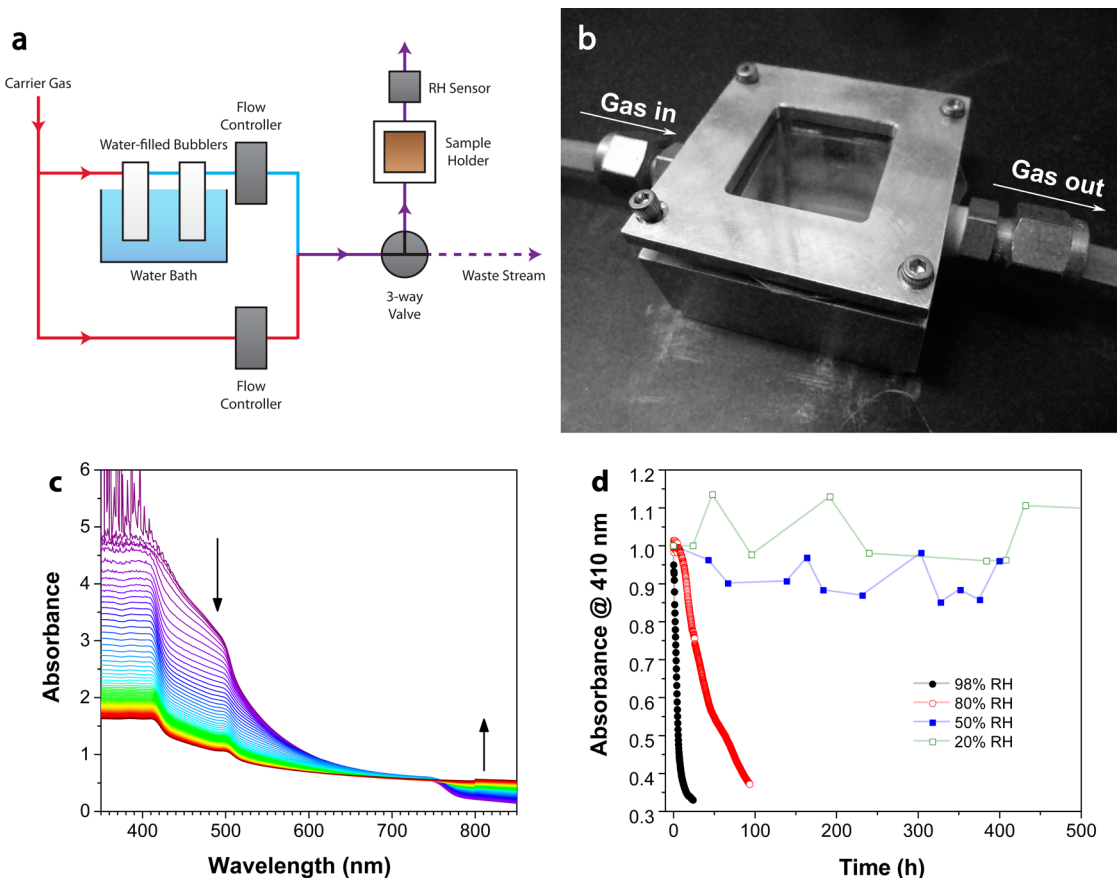


Figure 1. (a) Schematic of the RH control apparatus. (b) Sample holder for *in situ* UV–vis spectroscopy. (c) UV–vis spectra, acquired at 15 min intervals, of a $\text{CH}_3\text{NH}_3\text{PbI}_3$ film exposed to flowing N_2 gas with $\text{RH} = 98 \pm 2\%$. (d) Normalized absorbance at 410 nm as a function of time for perovskite films exposed to various relative humidities. Data at 50% and 20% RH were acquired once per 24 h. The temperature was measured to be $22.9 \pm 0.5^\circ\text{C}$ for all measurements.

determine whether various device components could serve a dual role, both as an important part of the actual device operation but also as a way of protecting the perovskite from moisture. In traditional perovskite solar cell designs, the hole transport layer covers the perovskite film, acting as a barrier between it and the ambient environment. As such, we chose to investigate three commonly used HTLs—2,2',7,7'-tetrakis(*N,N*-di-4-methoxyphenylamino)-9,9'-spirobifluorene (Spiro-OMeTAD), poly[bis(4-phenyl)(2,4,6-trimethylphenyl)amine] (PTAA), and poly(3-hexylthiophene) (P3HT)—in order to determine how the identity of the HTL affects the rate of perovskite degradation. Since these HTLs are often p-doped in order to increase the carrier density and reduce the device series resistance,^{25,37–42} we investigated each of the HTLs both with and without a lithium bis(trifluoromethanesulfonyl)imide (Li-TFSI) dopant.⁸ The $\text{CH}_3\text{NH}_3\text{PbI}_3/\text{HTL}$ bilayers were then exposed to a 98% RH atmosphere, and absorbance spectra were acquired every 15 min (Figure S5). The normalized absorbance at 410 nm is plotted as a function of time (Figure 2) and compared with the decomposition rate of an uncoated perovskite film. The measurements were done in duplicate (Figure S5d and e) in order to provide evidence of the reproducibility of the degradation

process. On the basis of the data, the identity of the HTL (with Li-TFSI dopant) clearly affects its ability to protect the underlying perovskite film: $\tau_{1/2} \approx 1, 7$, and 25 h for Spiro-OMeTAD, PTAA, and P3HT, respectively (compared with $\tau_{1/2} \approx 4$ h for the uncoated perovskite). Spiro-OMeTAD appears to accelerate the perovskite decomposition process, whereas both PTAA and P3HT appear to act as barriers to moisture ingress, with the P3HT providing a 6-fold improvement in the rate of decomposition. The shape of the decay profile was also different in each case. The uncoated perovskite film appeared to undergo a smooth transformation into reaction byproducts, whereas in the case of both the Spiro-OMeTAD- and PTAA-coated films, there was a sharp discontinuity in the absorbance data, after which the rate of decomposition increased dramatically. In contrast, the P3HT-coated film was stable for well over half a day before showing any sign of decomposition; however, after the *ca.* 15 h induction period, the perovskite film again appeared to decompose smoothly into reaction byproducts.

For analogous films prepared without the use of the Li-TFSI dopant, these differences are surprisingly less pronounced, with $\tau_{1/2} \approx 4, 6$, and 6 h for Spiro-OMeTAD, PTAA, and P3HT, respectively (Figure 2b).

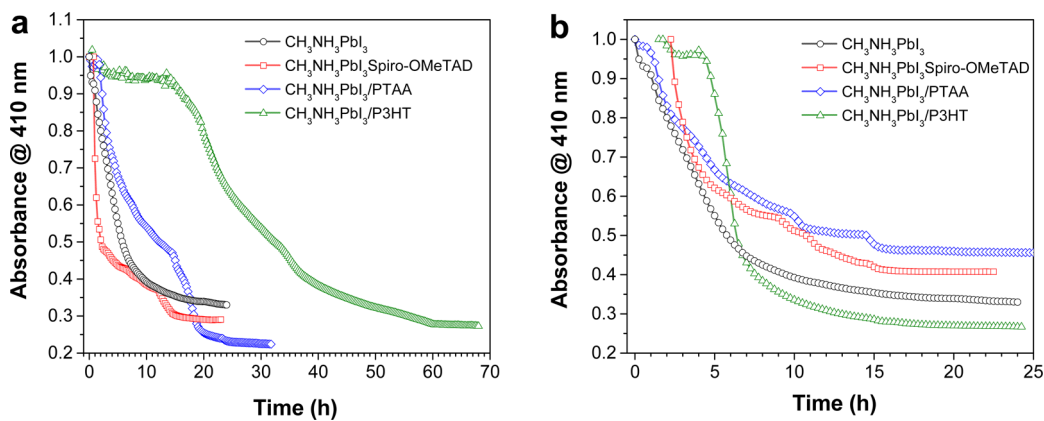


Figure 2. Normalized absorbance at 410 nm as a function of time for $\text{CH}_3\text{NH}_3\text{PbI}_3$ (open circles) and $\text{CH}_3\text{NH}_3\text{PbI}_3/\text{HTL}$ films, both with (a) and without (b) Li-TFSI dopants: $\text{CH}_3\text{NH}_3\text{PbI}_3/\text{Spiro-OMeTAD}$ (open squares), $\text{CH}_3\text{NH}_3\text{PbI}_3/\text{PTAA}$ (open diamonds), and $\text{CH}_3\text{NH}_3\text{PbI}_3/\text{P3HT}$ (open triangles) films exposed to a $98 \pm 2\%$ RH environment at $22.8 \pm 0.5^\circ\text{C}$.

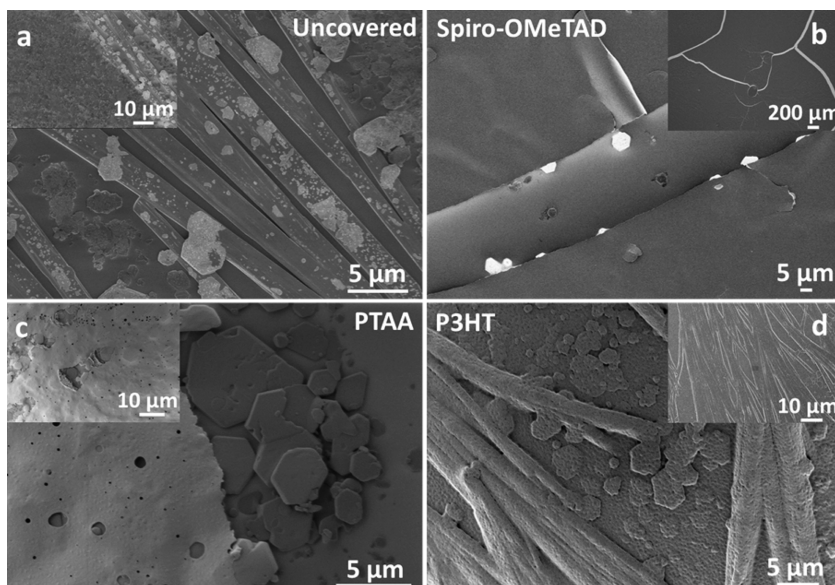


Figure 3. SEM images of (a) uncoated $\text{CH}_3\text{NH}_3\text{PbI}_3$, (b) $\text{CH}_3\text{NH}_3\text{PbI}_3/\text{Spiro-OMeTAD}$, (c) $\text{CH}_3\text{NH}_3\text{PbI}_3/\text{PTAA}$, and $\text{CH}_3\text{NH}_3\text{PbI}_3/\text{P3HT}$ films after exposure to 98% RH for 24 h.

From these data, it would appear that the doped P3HT layer actually slows the permeation of water through the polymer film. This data can best be understood in terms of a model that consists of a semipermeable P3HT film; in this scenario, water vapor is able to slowly percolate through the polymer, eventually reaching the perovskite and leading to decomposition. The more hydrophilic the HTL film, the more water vapor is trapped in the barrier polymer and the slower it migrates through the film. In the absence of the Li-TFSI salt, the P3HT is unable to adsorb much moisture and instead allows the water vapor to bleed through into the underlying perovskite film.

In order to better explain the differences between the various HTLs, the surfaces of the degraded $\text{CH}_3\text{NH}_3\text{PbI}_3/\text{HTL}$ films were imaged by scanning electron microscopy (Figure 3). After decomposition, the uncovered perovskite film appeared to have formed

large, hexagonal plates (consistent with previously reported morphologies for PbI_2 crystals^{43–45}) alongside dendritic, fibril-like structures (Figure 3a). The dendritic crystals are sufficiently large to be viewed with the naked eye (Figure S6), and on the basis of their dark brown color, they appear to be consistent with an evolution of the $\text{CH}_3\text{NH}_3\text{PbI}_3$ morphology. In the case of the Spiro-OMeTAD-coated films, very little of the underlying perovskite film can be seen; however, hexagonal PbI_2 crystals can still be observed. Most importantly, the Spiro-OMeTAD layer appears to have broken apart into individual pieces through substantial crack formation at the surface (Figure 3b). Similarly, for the PTAA-coated films, a number of large (0.1–10 μm) pinholes developed in the PTAA barrier layer (Figure 4c); the edges of some of these holes appear to have eroded into large gaps in the film, again exposing the large PbI_2 crystals underneath. Given the large volume changes

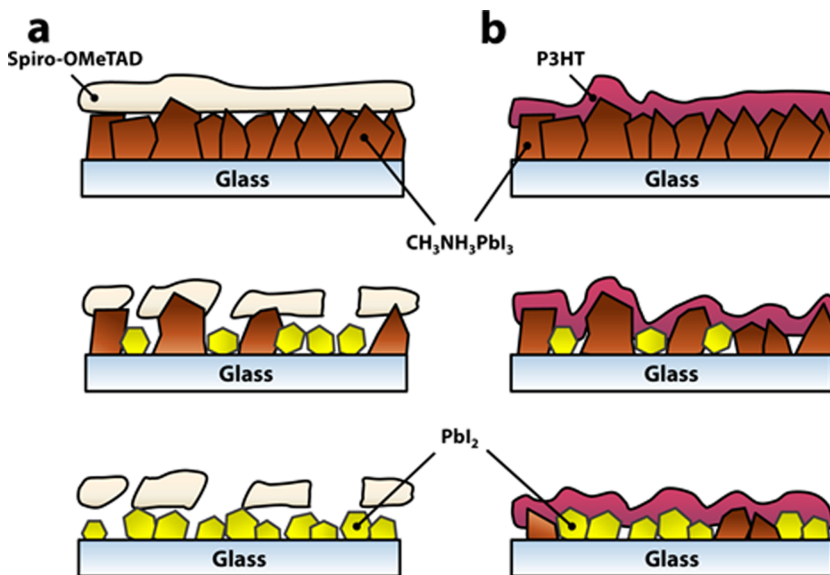


Figure 4. Cartoon depiction of the structural and morphological differences between (a) Spiro-OMeTAD and (b) P3HT HTLs upon exposure to water vapor.

associated with formation (and decomposition) of the perovskite films⁴⁶ and the resulting mechanical stress placed on the HTL, the failure of the HTL is perhaps unsurprising; the small molecule Spiro-OMeTAD lacks the mechanical toughness of a polymer, leading to substantial cracking of the film (Figure 4). Similarly, the relatively low molecular weight PTAA ($M_n \approx 7\text{--}10$ kDa), while mechanically more robust than Spiro-OMeTAD, rapidly crumbles as the underlying perovskite support is removed. This mechanical fracture of the HTL explains the discontinuities observed in the decomposition kinetics (Figure 2); as the HTL begins to break down, the rate of perovskite decomposition increases.

In contrast to both Spiro-OMeTAD and PTAA, P3HT actually appeared to function as a viable barrier layer, with a *ca.* 15 h induction period required to induce the start of perovskite decomposition. The origins of the improved performance of P3HT can be understood based on the images in Figure 3d and are illustrated in Figure 4b. P3HT forms dense, relatively crystalline films due to interdigitation and lamellar packing of the regioregular alkyl chains; however, due to the moderate molecular weight ($M_n \approx 50\text{--}70$ kDa), the films are still relatively easy to deform. As a result, the P3HT adheres conformally to the underlying perovskite layer throughout all phases of the decomposition, eventually forming a thick film on top of the hexagonal PbI₂ plates and dendritic byproducts (Figure 3d).

Although the *in situ* absorbance measurements provide a convenient spectroscopic handle by which to track the film degradation kinetics, they provide no structural information on changes in crystallinity or phase that occur during the decomposition process. As such, *ex situ* powder X-ray diffraction (pXRD) experiments were carried out in order to identify both the

initial perovskite phase and the identity of any crystalline decomposition products (Figure S7). The diffraction pattern of the as-prepared CH₃NH₃PbI₃ film is consistent with the tetragonal perovskite phase, crystallizing in the $I4cm$ space group.¹³ In addition to the reflections due to the tetragonal CH₃NH₃PbI₃, the powder diffraction pattern also revealed the presence of PbI₂ that was unconverted to the perovskite during the CH₃NH₃I intercalation step, as evidenced by the (001) and (10 $\bar{1}$) reflections at 14.5° and 29.6°, respectively.⁴⁷ A small amount of residual PbI₂ is often observed in perovskite thin films prepared using the two-step deposition process.^{8,48,49}

The *ex situ* pXRD results are entirely consistent with the UV-vis and SEM data, which show the decomposition of CH₃NH₃PbI₃ into PbI₂. However, in order to complement the *in situ* absorbance measurements and to better elucidate the reaction mechanism for the decomposition process, we carried out *in situ* GIXRD measurements on a perovskite film subjected to *ca.* 80% RH (Figure S8). The combination of a fast 2D area detector with a high brightness synchrotron X-ray source allows the acquisition of 2D diffraction data in real time, providing important insight into the decomposition process. Snapshots of the *in situ* GIXRD experiments at various time points are shown in Figure 5, with the whole 5.5 h of data combined into Movie S1 (shown at 412× normal speed). All of the GIXRD patterns exhibited a relatively strong scattering background from the amorphous glass substrate in the range of $q = 10\text{--}23$ nm⁻¹, where q is the scattering vector ($q = 4\pi \sin(\theta)/\lambda$). The contribution from the glass substrate is likely the result of the shallow angle of incidence ($\theta \approx 0.2^\circ$) and a large beam size in the vertical dimension. After calibration, key features of the perovskite diffraction pattern could be observed

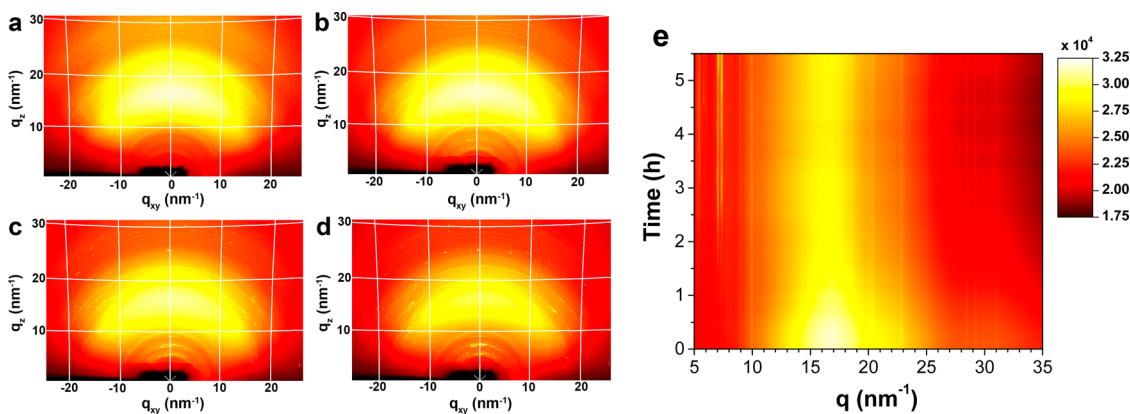


Figure 5. 2D GIXRD patterns of perovskite films on glass, after (a) 0 h, (b) 2 h, (c) 4 h, and (d) 5.5 h exposure to an 80% RH environment. (e) 2D contour plot showing the azimuthally integrated diffraction intensity as a function of both scattering vector (q) and time.

at $q \approx 10, 20, 23, 29, and 31 nm^{-1} , consistent with reflection from the (110), (220), (310), (224), and (314) lattice planes, respectively. Additional features ($q \approx 9$ and 28 nm^{-1}) could be assigned to reflections from the (001) and (2̄10) planes of PbI_2 ,^{18,50,51} consistent with the data obtained from benchtop pXRD experiments (Figure S7). As the film was exposed to moisture, additional diffraction spots began to appear at ca. $q \approx 5$ and 7 nm^{-1} , eventually forming a more complete ring pattern as the decomposition process continued. The azimuthally integrated intensity of the *in situ* GIXRD data is plotted as a function of both scattering vector and time in Figure 5e. The new features in the diffraction pattern at 5 and 7 nm^{-1} appear after ca. 2.5 h and cannot be assigned to either $\text{CH}_3\text{NH}_3\text{PbI}_3$, PbI_2 , or $\text{CH}_3\text{NH}_3\text{I}$. This suggests that a new crystalline phase forms as an intermediate during the reaction of the perovskite film with water vapor. Although we cannot conclusively identify the origin of these small-angle diffraction features, previous work has structurally characterized the hydrated compound $(\text{CH}_3\text{NH}_3)_4\text{PbI}_6 \cdot 2\text{H}_2\text{O}$, which was isolated from an aqueous solution of $\text{CH}_3\text{NH}_3\text{I}$ and PbI_2 .⁵² This yellow crystalline hydrate consists of isolated PbI_6^{4-} octahedra and is predicted to show a diffraction peak at $q \approx 8\text{ nm}^{-1}$. While this does not entirely agree with the data shown in Figure 5e, it does suggest the possibility of a hydrated phase with isolated PbI_6^{4-} octahedra—either $(\text{CH}_3\text{NH}_3)_4\text{PbI}_6 \cdot 2\text{H}_2\text{O}$ or a related compound—acting as an intermediate in the decomposition pathway of $\text{CH}_3\text{NH}_3\text{PbI}_3$.$

Further evidence for this intermediate hydrate phase was obtained from experiments conducted on a bulk sample of $\text{CH}_3\text{NH}_3\text{PbI}_3$ powder. The sample of bulk $\text{CH}_3\text{NH}_3\text{PbI}_3$ was first prepared by dissolving $\text{CH}_3\text{NH}_3\text{I}$ and PbI_2 in DMF in a 1:1 mol ratio, followed by evaporation of the solvent, drying at 120°C for 1 h in an oven, and grinding the resultant solid into powder. The sample was determined to be phase pure by powder X-ray diffraction (Figure 6). A small amount of water (60 μL) was then added to the perovskite

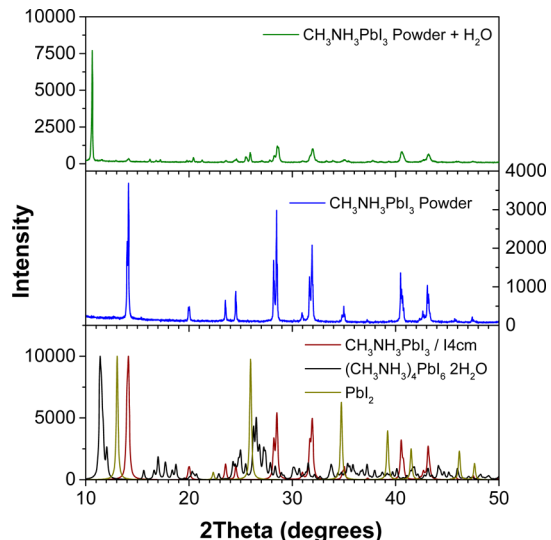


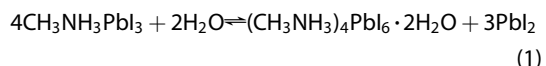
Figure 6. Powder X-ray diffraction patterns for a sample of $\text{CH}_3\text{NH}_3\text{PbI}_3$ powder, before (blue line) and after (green line) the addition of a small amount of liquid water. The calculated powder patterns for tetragonal $\text{CH}_3\text{NH}_3\text{PbI}_3$ (dark red line), $(\text{CH}_3\text{NH}_3)_4\text{PbI}_6 \cdot 2\text{H}_2\text{O}$ (black line), and PbI_2 (yellow line) are shown for comparison. Data were acquired (or simulated) using a copper X-ray source ($\lambda = 1.54\text{ \AA}$).

sample (200 mg) and homogenized by grinding in a mortar and pestle. The powder X-ray diffraction pattern of the resulting pale yellow powder showed that there was no PbI_2 present; rather, the sample appeared to consist of a mixture of $(\text{CH}_3\text{NH}_3)_4\text{PbI}_6 \cdot 2\text{H}_2\text{O}$ and a small amount of residual $\text{CH}_3\text{NH}_3\text{PbI}_3$. Assuming that the adsorption of liquid water by the bulk perovskite powder is likely to produce a very similar product to the adsorption of water vapor by a perovskite thin film; this indicates that the low-angle features observed in the GIXRD data are likely to be either $(\text{CH}_3\text{NH}_3)_4\text{PbI}_6 \cdot 2\text{H}_2\text{O}$ or a very closely related hydrate. The hydrated phase was unstable in room air and was found to revert back to the perovskite over a period of several tens of minutes.

This intermediate hydrated phase is in contrast to previous work by Niu *et al.*,²⁸ who suggested that the

first step of the perovskite decomposition pathway is the deprotonation of the methylammonium cation by water, forming methylamine, hydrated Hl , and Pbl_2 . If this hypothesis is correct, one would expect that the volatile CH_3NH_2 would be rapidly flushed from the headspace of our *in situ* sample holder, meaning the process would be unlikely to be reversible. Given the apparent reversibility in the bulk powder, it was expected that thin films would also display similar reversible conversion to the hydrate phase. A fresh perovskite film was therefore mounted in our *in situ* absorbance spectroscopy sample chamber and exposed to a flow of $98 \pm 2\%$ RH gas for a period of 24 h, and the headspace was subsequently flushed with dry nitrogen gas (0% RH). The absorbance spectra are shown in Figure S9. The initial decomposition proceeds as expected, and after 24 h, there is no evidence of any residual $\text{CH}_3\text{NH}_3\text{Pbl}_3$ (as measured by the lack of an optical band gap at 760 nm) and the film is bright yellow (Figure S9). However, after flushing with dry nitrogen, the film rapidly dehydrates, regenerating some of the dark brown color of $\text{CH}_3\text{NH}_3\text{Pbl}_3$. This is accompanied by a partial regeneration of the absorption edge at 760 nm (although the high-energy absorption bands typically associated with the $\text{CH}_3\text{NH}_3\text{Pbl}_3$ band structure do not reappear). The total dehydration process appears to take less than 1 min. This strongly suggests that the initial step of the perovskite decomposition process is not an acid–base reaction of the methylammonium cation, but rather hydration of the perovskite film (as illustrated in eq 1

with $(\text{CH}_3\text{NH}_3)_4\text{Pbl}_6 \cdot 2\text{H}_2\text{O}$, although other hydrate compositions may be possible):



Since eq 1 does not produce any volatile byproducts, it would be expected to be at least partially reversible; however, given the propensity of Pbl_2 to crystallize and phase separate (Figure 3), the process is unlikely to be fully reversible (which is consistent with the data in Figure S9). Further decomposition of $\text{CH}_3\text{NH}_3\text{I}$ to CH_3NH_2 and HI would ultimately leave Pbl_2 as the only byproduct of the reaction, in keeping with the *ex situ* pXRD data (Figure S7).

CONCLUSION

Through the application of both *in situ* absorbance spectroscopy and *in situ* GIXRD measurements, we have been able to quantitatively and reproducibly evaluate the stability of $\text{CH}_3\text{NH}_3\text{Pbl}_3$ films. We show that the identity of the hole transport layer can have a dramatic impact on the stability of the underlying perovskite film, suggesting a route toward perovskite solar cells with long device lifetimes and a resistance to humidity. The *in situ* GIXRD measurements suggest the formation of a hydrated intermediate containing isolated Pbl_6^{4-} octahedra as the first step in the decomposition process. These results help elucidate fundamental decomposition pathways in organolead halide perovskite films, which is expected to in turn lead to more stable materials and more commercially viable devices.

METHODS

Film Formation. All films were fabricated on precleaned glass substrates. Pbl_2 films were deposited by spin coating a $460 \text{ mg} \cdot \text{mL}^{-1}$ solution of Pbl_2 in *N,N*-dimethylformamide at 3000 rpm for 15 s. Perovskite films were obtained by dipping the as-cast Pbl_2 films into a $10 \text{ mg} \cdot \text{mL}^{-1}$ solution of $\text{CH}_3\text{NH}_3\text{I}$ in 2-propanol for 2 min. P3HT was deposited by spin coating from chlorobenzene solution (20 mg of P3HT, $3.4 \mu\text{L}$ of 4-*tert*-butylpyridine, and $6.8 \mu\text{L}$ of Li-TFSI solution (28 mg Li-TFSI/ 1 mL acetonitrile) all dissolved in 1 mL of chlorobenzene) at 1000 rpm at 25 s. Spiro-OMeTAD was deposited by spin coating from chlorobenzene solution (80 mg of Spiro-OMeTAD, $28.5 \mu\text{L}$ of 4-*tert*-butylpyridine, and $17.5 \mu\text{L}$ of Li-TFSI solution (520 mg Li-TFSI/ 1 mL acetonitrile) all dissolved in 1 mL of chlorobenzene) at 2000 rpm for 25 s. PTAA was deposited by spin coating from chlorobenzene solution (20 mg of PTAA, $7.5 \mu\text{L}$ of 4-*tert*-butylpyridine, and $15 \mu\text{L}$ of Li-TFSI solution (170 mg Li-TFSI/ 1 mL acetonitrile) all dissolved in 1 mL of chlorobenzene) at 2000 rpm for 25 s. All films were stored in a N_2 -atmosphere glovebox ($<0.1 \text{ ppm}$ of O_2 and H_2O) prior to measurements.

Characterization. Scanning electron microscopy was carried out on a Hitachi SU8010 instrument operating at a 0.1 – 1.0 kV landing voltage. Powder X-ray diffraction was performed on a PANalytical Empyrean diffractometer configured with either a copper (Figure 6, $\lambda = 1.54 \text{ \AA}$) or cobalt (Figure S7, $\lambda = 1.79 \text{ \AA}$) X-ray source. UV–vis absorbance spectra were acquired on a Cary 6000i spectrophotometer. The films were measured in a custom-built sample holder, and the RH was measured using a humidity sensor (RH-USB, Omega).

GIXRD Measurements. GIXRD measurements were conducted at the Hard X-ray MicroAnalysis (HXMA) beamline of the Canadian Light Source (CLS). An energy of 17.998 keV ($\lambda = 0.6888 \text{ \AA}$) was selected using a Si(111) monochromator. GIXRD patterns were collected on a SX165 CCD camera (Rayonix) placed at a distance of 141 mm from the sample using a 30 s acquisition time. A lead beamstop was used to block the direct beam. For *in situ* experiments, the films were placed in a sample chamber sealed with a Kapton window, and GIXRD patterns were collected every 30 s. CCD images were processed using the Datasqueeze 3.0 software package.

Conflict of Interest: The authors declare no competing financial interest.

Supporting Information Available: Supplementary *in situ* and *ex situ* UV–vis spectra, kinetic data, pXRD patterns, photographs of degraded perovskite films, schematic of the GIXRD experimental setup. This material is available free of charge via the Internet at <http://pubs.acs.org>.

Acknowledgment. Research described in this paper was performed at the Canadian Light Source, which is supported by the Canada Foundation for Innovation, the Natural Sciences and Engineering Research Council of Canada (NSERC), the University of Saskatchewan, the Government of Saskatchewan, Western Economic Diversification Canada, the National Research Council Canada, and the Canadian Institutes of Health Research. Technical support from HXMA beamline scientist Dr. Chang-Yong Kim is gratefully acknowledged. NSERC and the University of Saskatchewan are acknowledged for financial

support. T.L.K. is a Canada Research Chair in Photovoltaics. The research was undertaken, in part, thanks to funding from the Canada Research Chair program. B.D.S. thanks the Inorganic Chemistry Exchange (ICE) program and NSERC for an Undergraduate Student Research Award (USRA). Dr. Dongniu Wang and Mr. Mahesh Gangishetty are gratefully acknowledged for assistance with the GIXRD experiments and the powder X-ray diffraction measurements, respectively.

REFERENCES AND NOTES

- Kojima, A.; Teshima, K.; Shirai, Y.; Miyasaka, T. Organometal Halide Perovskites as Visible-Light Sensitizers for Photovoltaic Cells. *J. Am. Chem. Soc.* **2009**, *131*, 6050–6051.
- Xiao, Z. G.; Bi, C.; Shao, Y. C.; Dong, Q. F.; Wang, Q.; Yuan, Y. B.; Wang, C. G.; Gao, Y. L.; Huang, J. S. Efficient, High Yield Perovskite Photovoltaic Devices Grown by Interdiffusion of Solution-Processed Precursor Stacking Layers. *Energy Environ. Sci.* **2014**, *7*, 2619–2623.
- Wojciechowski, K.; Saliba, M.; Leijtens, T.; Abate, A.; Snaith, H. J. Sub-150 Degrees C Processed Meso-Superstructured Perovskite Solar Cells with Enhanced Efficiency. *Energy Environ. Sci.* **2014**, *7*, 1142–1147.
- Wang, Q.; Shao, Y. C.; Dong, Q. F.; Xiao, Z. G.; Yuan, Y. B.; Huang, J. S. Large Fill-Factor Bilayer Iodine Perovskite Solar Cells Fabricated by a Low-Temperature Solution-Process. *Energy Environ. Sci.* **2014**, *7*, 2359–2365.
- Jeon, N. J.; Lee, H. G.; Kim, Y. C.; Seo, J.; Noh, J. H.; Lee, J.; Seok, S. I. O-Methoxy Substituents in Spiro-OMetad for Efficient Inorganic–Organic Hybrid Perovskite Solar Cells. *J. Am. Chem. Soc.* **2014**, *136*, 7837–7840.
- Ryu, S.; Noh, J. H.; Jeon, N. J.; Kim, Y. C.; Yang, S.; Seo, J. W.; Seok, S. I. Voltage Output of Efficient Perovskite Solar Cells with High Open-Circuit Voltage and Fill Factor. *Energy Environ. Sci.* **2014**, *7*, 2614–2618.
- Liu, M. Z.; Johnston, M. B.; Snaith, H. J. Efficient Planar Heterojunction Perovskite Solar Cells by Vapour Deposition. *Nature* **2013**, *501*, 395–398.
- Burschka, J.; Pellet, N.; Moon, S. J.; Humphry-Baker, R.; Gao, P.; Nazeeruddin, M. K.; Gratzel, M. Sequential Deposition as a Route to High-Performance Perovskite-Sensitized Solar Cells. *Nature* **2013**, *499*, 316–319.
- Jeon, N. J.; Noh, J. H.; Kim, Y. C.; Yang, W. S.; Ryu, S.; Seol, S. I. Solvent Engineering for High-Performance Inorganic–Organic Hybrid Perovskite Solar Cells. *Nat. Mater.* **2014**, *13*, 897–903.
- Zhou, H. P.; Chen, Q.; Li, G.; Luo, S.; Song, T. B.; Duan, H. S.; Hong, Z. R.; You, J. B.; Liu, Y. S.; Yang, Y. Interface Engineering of Highly Efficient Perovskite Solar Cells. *Science* **2014**, *345*, 542–546.
- Green, M. A.; Emery, K.; Hishikawa, Y.; Warta, W.; Dunlop, E. D. Solar Cell Efficiency Tables (Version 44). *Prog. Photovoltaics* **2014**, *22*, 701–710.
- Wehrenfennig, C.; Eperon, G. E.; Johnston, M. B.; Snaith, H. J.; Herz, L. M. High Charge Carrier Mobilities and Lifetimes in Organolead Trihalide Perovskites. *Adv. Mater.* **2014**, *26*, 1584–1589.
- Stoumpos, C. C.; Malliakas, C. D.; Kanatzidis, M. G. Semiconducting Tin and Lead Iodide Perovskites with Organic Cations: Phase Transitions, High Mobilities, and near-Infrared Photoluminescent Properties. *Inorg. Chem.* **2013**, *52*, 9019–9038.
- Ponseca, C. S.; Savenije, T. J.; Abdellah, M.; Zheng, K. B.; Yartsev, A.; Pascher, T.; Harlang, T.; Chabera, P.; Pullerits, T.; Stepanov, A.; et al. Organometal Halide Perovskite Solar Cell Materials Rationalized: Ultrafast Charge Generation, High and Microsecond-Long Balanced Mobilities, and Slow Recombination. *J. Am. Chem. Soc.* **2014**, *136*, 5189–5192.
- Xing, G. C.; Mathews, N.; Sun, S. Y.; Lim, S. S.; Lam, Y. M.; Gratzel, M.; Mhaisalkar, S.; Sum, T. C. Long-Range Balanced Electron- and Hole-Transport Lengths in Organic-Inorganic $\text{CH}_3\text{NH}_3\text{PbI}_3$. *Science* **2013**, *342*, 344–347.
- Etgari, L.; Gao, P.; Xue, Z. S.; Peng, Q.; Chandiran, A. K.; Liu, B.; Nazeeruddin, M. K.; Gratzel, M. Mesoscopic $\text{CH}_3\text{NH}_3\text{PbI}_3/\text{TiO}_2$ Heterojunction Solar Cells. *J. Am. Chem. Soc.* **2012**, *134*, 17396–17399.
- Ball, J. M.; Lee, M. M.; Hey, A.; Snaith, H. J. Low-Temperature Processed Meso-Superstructured to Thin-Film Perovskite Solar Cells. *Energy Environ. Sci.* **2013**, *6*, 1739–1743.
- Lee, M. M.; Teuscher, J.; Miyasaka, T.; Murakami, T. N.; Snaith, H. J. Efficient Hybrid Solar Cells Based on Meso-Superstructured Organometal Halide Perovskites. *Science* **2012**, *338*, 643–647.
- Liu, D. Y.; Kelly, T. L. Perovskite Solar Cells with a Planar Heterojunction Structure Prepared Using Room-Temperature Solution Processing Techniques. *Nat. Photonics* **2014**, *8*, 133–138.
- Hodes, G.; Cahen, D. Photovoltaics: Perovskite Cells Roll Forward. *Nat. Photonics* **2014**, *8*, 87–88.
- Malinkiewicz, O.; Yella, A.; Lee, Y. H.; Espallargas, G. M.; Graetzel, M.; Nazeeruddin, M. K.; Bolink, H. J. Perovskite Solar Cells Employing Organic Charge-Transport Layers. *Nat. Photonics* **2014**, *8*, 128–132.
- Noel, N. K.; Stranks, S. D.; Abate, A.; Wehrenfennig, C.; Guarnera, S.; Haghhighirad, A. A.; Sadhanala, A.; Eperon, G. E.; Pathak, S. K.; Johnston, M. B.; et al. Lead-Free Organic-Inorganic Tin Halide Perovskites for Photovoltaic Applications. *Energy Environ. Sci.* **2014**, *7*, 3061–3068.
- Hao, F.; Stoumpos, C. C.; Cao, D. H.; Chang, R. P. H.; Kanatzidis, M. G. Lead-Free Solid-State Organic-Inorganic Halide Perovskite Solar Cells. *Nat. Photonics* **2014**, *8*, 489–494.
- Zhao, Y. X.; Zhu, K. Optical Bleaching of Perovskite ($\text{CH}_3\text{NH}_3\text{PbI}_3$) through Room-Temperature Phase Transformation Induced by Ammonia. *Chem. Commun.* **2014**, *50*, 1605–1607.
- Habisreutinger, S. N.; Leijtens, T.; Eperon, G. E.; Stranks, S. D.; Nicholas, R. J.; Snaith, H. J. Carbon Nanotube/Polymer Composites as a Highly Stable Hole Collection Layer in Perovskite Solar Cells. *Nano Lett.* **2014**, *14*, 5561–5568.
- Christians, J. A.; Miranda Herrera, P. A.; Kamat, P. V. Transformation of the Excited State and Photovoltaic Efficiency of $\text{CH}_3\text{NH}_3\text{PbI}_3$ Perovskite Upon Controlled Exposure to Humidified Air. *J. Am. Chem. Soc.* **2015**, *137*, 1530–1538.
- Clever, H. L.; Johnston, F. J. The Solubility of Some Sparingly Soluble Lead Salts - an Evaluation of the Solubility in Water and Aqueous-Electrolyte Solution. *J. Phys. Chem. Ref. Data* **1980**, *9*, 751–784.
- Niu, G. D.; Li, W. Z.; Meng, F. Q.; Wang, L. D.; Dong, H. P.; Qiu, Y. Study on the Stability of $\text{CH}_3\text{NH}_3\text{PbI}_3$ Films and the Effect of Post-Modification by Aluminum Oxide in All-Solid-State Hybrid Solar Cells. *J. Mater. Chem. A* **2014**, *2*, 705–710.
- Zheng, L.; Chung, Y. H.; Ma, Y.; Zhang, L.; Xiao, L.; Chen, Z.; Wang, S.; Qu, B.; Gong, Q. A Hydrophobic Hole Transporting Oligothiophene for Planar Perovskite Solar Cells with Improved Stability. *Chem. Commun.* **2014**, *50*, 11196–11199.
- Smith, I. C.; Hoke, E. T.; Solis-Ibarra, D.; McGehee, M. D.; Karunadasa, H. I. A Layered Hybrid Perovskite Solar-Cell Absorber with Enhanced Moisture Stability. *Angew. Chem., Int. Ed.* **2014**, *53*, 11232–11235.
- Noh, J. H.; Im, S. H.; Heo, J. H.; Mandal, T. N.; Seok, S. I. Chemical Management for Colorful, Efficient, and Stable Inorganic–Organic Hybrid Nanostructured Solar Cells. *Nano Lett.* **2013**, *13*, 1764–1769.
- Mei, A.; Li, L.; Liu, L.; Ku, Z.; Liu, T.; Rong, Y.; Xu, M.; Hu, M.; Chen, J.; Yang, Y.; et al. A Hole-Conductor-Free, Fully Printable Mesoscopic Perovskite Solar Cell with High Stability. *Science* **2014**, *345*, 295–298.
- Zhang, F. Q.; Yang, X. C.; Wang, H. X.; Cheng, M.; Zhao, J. H.; Sun, L. C. Structure Engineering of Hole-Conductor Free Perovskite-Based Solar Cells with Low-Temperature-Processed Commercial Carbon Paste as Cathode. *ACS Appl. Mater. Interfaces* **2014**, *6*, 16140–16146.
- Wei, Z.; Chen, H.; Yan, K.; Yang, S. Inkjet Printing and Instant Chemical Transformation of a $\text{CH}_3\text{NH}_3\text{PbI}_3/\text{Nanocarbon}$ Electrode and Interface for Planar Perovskite Solar Cells. *Angew. Chem., Int. Ed.* **2014**, *53*, 13239–13243.

35. Zhou, H. W.; Shi, Y. T.; Dong, Q. S.; Zhang, H.; Xing, Y. J.; Wang, K.; Du, Y.; Ma, T. L. Hole-Conductor-Free, Metal-Electrode-Free $\text{TiO}_2/\text{CH}_3\text{NH}_3\text{PbI}_3$ Heterojunction Solar Cells Based on a Low-Temperature Carbon Electrode. *J. Phys. Chem. Lett.* **2014**, *5*, 3241–3246.
36. Mie, G. Beitrag Zur Optik Truber Medien Speziell Kolloidaler Metallösungen. *Ann. Phys.* **1908**, *25*, 377–445.
37. Heo, J. H.; Im, S. H.; Noh, J. H.; Mandal, T. N.; Lim, C. S.; Chang, J. A.; Lee, Y. H.; Kim, H. J.; Sarkar, A.; Nazeeruddin, M. K.; et al. Efficient Inorganic-Organic Hybrid Heterojunction Solar Cells Containing Perovskite Compound and Polymeric Hole Conductors. *Nat. Photonics* **2013**, *7*, 486–491.
38. Dualeh, A.; Moehl, T.; Nazeeruddin, M. K.; Gratzel, M. Temperature Dependence of Transport Properties of Spiro-Meotad as a Hole Transport Material in Solid-State Dye-Sensitized Solar Cells. *ACS Nano* **2013**, *7*, 2292–2301.
39. Abate, A.; Hollman, D. J.; Teuscher, J.; Pathak, S.; Avolio, R.; D'Errico, G.; Vitiello, G.; Fantacci, S.; Snaith, H. J. Proton Ionic Liquids as P-Dopant for Organic Hole Transporting Materials and Their Application in High Efficiency Hybrid Solar Cells. *J. Am. Chem. Soc.* **2013**, *135*, 13538–13548.
40. Burschka, J.; Dualeh, A.; Kessler, F.; Baranoff, E.; Cevey-Ha, N. L.; Yi, C. Y.; Nazeeruddin, M. K.; Gratzel, M. Tris(2-(1H-Pyrazol-1-Yl)Pyridine)Cobalt(III) as P-Type Dopant for Organic Semiconductors and Its Application in Highly Efficient Solid-State Dye-Sensitized Solar Cells. *J. Am. Chem. Soc.* **2011**, *133*, 18042–18045.
41. Leijtens, T.; Lim, J.; Teuscher, J.; Park, T.; Snaith, H. J. Charge Density Dependent Mobility of Organic Hole-Transporters and Mesoporous TiO_2 Determined by Transient Mobility Spectroscopy: Implications to Dye-Sensitized and Organic Solar Cells. *Adv. Mater.* **2013**, *25*, 3227–3233.
42. Di Giacomo, F.; Razza, S.; Matteocci, F.; D'Epifanio, A.; Licoccia, S.; Brown, T. M.; Di Carlo, A. High Efficiency $\text{CH}_3\text{NH}_3\text{PbI}_{(3-x)}\text{Cl}_x$ Perovskite Solar Cells with Poly-(3-Hexylthiophene) Hole Transport Layer. *J. Power Sources* **2014**, *251*, 152–156.
43. Zheng, Z.; Liu, A. R.; Wang, S. M.; Wang, Y.; Li, Z. S.; Lau, W. M.; Zhang, L. Z. In Situ Growth of Epitaxial Lead Iodide Films Composed of Hexagonal Single Crystals. *J. Mater. Chem.* **2005**, *15*, 4555–4559.
44. Nayak, A.; Bhalla, G. L.; Trigunayat, G. C. Laser-Induced Energy Gap Transitions in Lead Iodide Crystals. *Mater. Res. Bull.* **2000**, *35*, 2263–2273.
45. Oliveira, I. B.; Costa, F. E.; Armelin, M. J.; Cardoso, L. P.; Hamada, M. M. Purification and Growth of PbI_2 Crystals - Dependence of the Radiation Response on the PbI_2 Crystal Purity. *IEEE Trans. Nucl. Sci.* **2002**, *49*, 1968–1973.
46. Liu, D.; Gangishetty, M. K.; Kelly, T. L. Effect of $\text{CH}_3\text{NH}_3\text{PbI}_3$ Thickness on Device Efficiency in Planar Heterojunction Perovskite Solar Cells. *J. Mater. Chem. A* **2014**, *2*, 19873–19881.
47. Terpstra, P.; Westenbrink, H. G. K. On the Crystal-Structure of Lead-Iodide. *P. K. Akad. Wet-Amsterd.* **1926**, *29*, 431–442.
48. Cao, D. H.; Stoumpos, C. C.; Malliakas, C. D.; Katz, M. J.; Farha, O. K.; Hupp, J. T.; Kanatzidis, M. G. Remnant PbI_2 , an Unforeseen Necessity in High-Efficiency Hybrid Perovskite-Based Solar Cells. *APL Mater.* **2014**, *2*, 091101.
49. Liu, D.; Yang, J.; Kelly, T. L. Compact Layer Free Perovskite Solar Cells with 13.5% Efficiency. *J. Am. Chem. Soc.* **2014**, *136*, 17116–17122.
50. Tan, K. W.; Moore, D. T.; Saliba, M.; Sai, H.; Estroff, L. A.; Hanrath, T.; Snaith, H. J.; Wiesner, U. Thermally Induced Structural Evolution and Performance of Mesoporous Block Copolymer-Directed Alumina Perovskite Solar Cells. *ACS Nano* **2014**, *8*, 4730–4739.
51. Colella, S.; Mosconi, E.; Fedeli, P.; Listorti, A.; Gazza, F.; Orlandi, F.; Ferro, P.; Besagni, T.; Rizzo, A.; Calestani, G.; et al. $\text{MAPbI}_{(3-x)}\text{Cl}_x$ Mixed Halide Perovskite for Hybrid Solar Cells: The Role of Chloride as Dopant on the Transport and Structural Properties. *Chem. Mater.* **2013**, *25*, 4613–4618.
52. Vincent, B. R.; Robertson, K. N.; Cameron, T. S.; Knop, O. Alkylammonium Lead Halides. 1. Isolated PbI_6^{4-} Ions in $(\text{CH}_3\text{NH}_3)_4\text{PbI}_6 \cdot 2\text{H}_2\text{O}$. *Can. J. Chem.* **1987**, *65*, 1042–1046.